Journal of Solid State Chemistry **142,** 89–99 (1999)
Article ID jssc.1998.7990, available online at http://www.idealibrary.com on IDEAL®

High-Resolution Electron Microscopy Investigations on the Real Structure of Reduced Barium Oxomolybdates

I. Polytypism and Chemical Intergrowth in $Ba_3Mo_{18}O_{28}$

R. Ramlau,[1] R. E. McCarley,* and A. Simon

Max-Planck-Institut für Festkörperforschung, Heisenbergstrasse 1, 70569 Stuttgart, Germany; and
** Ames Laboratory USDOE and Department of Chemistry, Iowa State University, Ames, Iowa 50011-3020*

Received April 21, 1998; in revised form July 29, 1998; accepted August 3, 1998

$Ba_3Mo_{18}O_{28}$, a reduced ternary molybdenum oxide in the series $M_{n\pm\delta}Mo_{4n+2}O_{6n+4}$ with $n = 4$, is a cluster compound containing $Mo_{4n+2}O_{8n+10}$ clusters with $n = 4$ *trans* edge-sharing molybdenum octahedra. Crystals of the compound were investigated by high-resolution electron microscopy (HREM), selected-area electron diffraction (SAD), and electron probe microanalysis. Besides the known monoclinic 1*M* modification of $Ba_3Mo_{18}O_{28}$ an orthorhombic 2*O* polytype was discovered, probably crystallizing in space group *Pnam*. Lattice parameters were estimated, and a rough structure model was generated. The real structure of $Ba_3Mo_{18}O_{28}$ is characterized by: (i) intergrowth of both ordered polytypes, 1*M* and 2*O*; (ii) stacking disorder; (iii) polysynthetic microtwinning of the 1*M* polytype; (iv) disordered chemical intergrowth of $Mo_{4n+2}O_{8n+10}$-cluster layers with $n = 2$, 3, and 5; and (v) chemical intergrowth of the phase $BaMo_6O_{10}$ (formally $n = 1$). In connection with particular defects, an irregular condensation of clusters was observed. Discrepancies between experimental HREM and SAD results and related computer simulations are discussed, as well as the reliability of X-ray structure results from defective single crystals. © 1999 Academic Press

INTRODUCTION

From the early days of high-resolution electron microscopy (HREM), solid state chemists were among the promoters of this method. A famous example of pioneer activities is the direct imaging of nonperiodic shear structures in transition-metal oxide systems, the so-called Wadsley defects (1). Nowadays, HREM has almost developed into a routine method of solid state chemistry. When applied to crystalline matter, HREM mainly aims at the real structure, whereas the ideal structure is usually investigated best by X-ray methods. Although the diverse phenomena of real structure seldom arouse the prime interest of solid state chemists, much valuable chemical information can be obtained when studying any deviation from the ideal structure. Sometimes it is even possible to prove the existence of new compounds or new modifications of already known compounds in microscopic regions, and chemists are inspired to prepare these products in single-phase form (2).

$Ba_3Mo_{18}O_{28}$, which has been prepared and structurally characterized by Schimek *et al.* (3), is a reduced molybdenum oxide containing $Mo_{18}O_{42}$ clusters (cf. Fig. 1a) with four *trans* edge-sharing molybdenum octahedra (4). $Ba_3Mo_{18}O_{28}$ belongs to a family of ternary and quaternary molybdenum oxides following the general formula $M_{n\pm\delta}Mo_{4n+2}O_{6n+4}$ with n indicating the number of *trans* edge-sharing molybdenum octahedra in the $Mo_{4n+2}O_{8n+10}$ clusters. Besides $Ba_3Mo_{18}O_{28}$ with $n = 4$, other representatives of the family are known with barium or mainly barium as countercations: $BaMo_6O_{10}$ with $n = 1$ (5), $K_{0.19}Ba_{3.81}Mo_{22}O_{34}$ with $n = 5$ (6), and $Ba_{0.62}Mo_4O_6$ with $n \to \infty$ (7, 8). The list of reduced molybdenum oxides lengthens by more representatives with different values of n when other countercations than barium are included. A complete overview is given elsewhere (9).

$Ba_{0.62}Mo_4O_6$, whose structure is closely related to that of $NaMo_4O_6$ (10), contains infinite chains of *trans* edge-sharing molybdenum octahedra. In the compounds with n being finite, (oligomeric) clusters are arranged in layers which may be regarded as slightly distorted cut–outs of the infinite chain structure, cut perpendicular to the chain axis. The top and bottom of each cluster layer are connected to adjacent layers via Mo–O–Mo bridges, as illustrated by Fig. 1b. This connection can vary such that the position of the adjacent top and bottom layers is either *cis*, like in $BaMo_6O_{10}$, or *trans*, like in $Ba_3Mo_{18}O_{28}$ and $K_{0.19}Ba_{3.81}Mo_{22}O_{34}$.

It might be a matter of interest from the very beginning that $BaMo_6O_{10}$ doubtlessly belongs to the mentioned family of oxides with respect to its inherent structural principle and the general formula, which is fulfilled for $n = 1$, thus indicating that there are no condensed but isolated

[1]To whom correspondence should be addressed.

0022-4596/99 $30.00

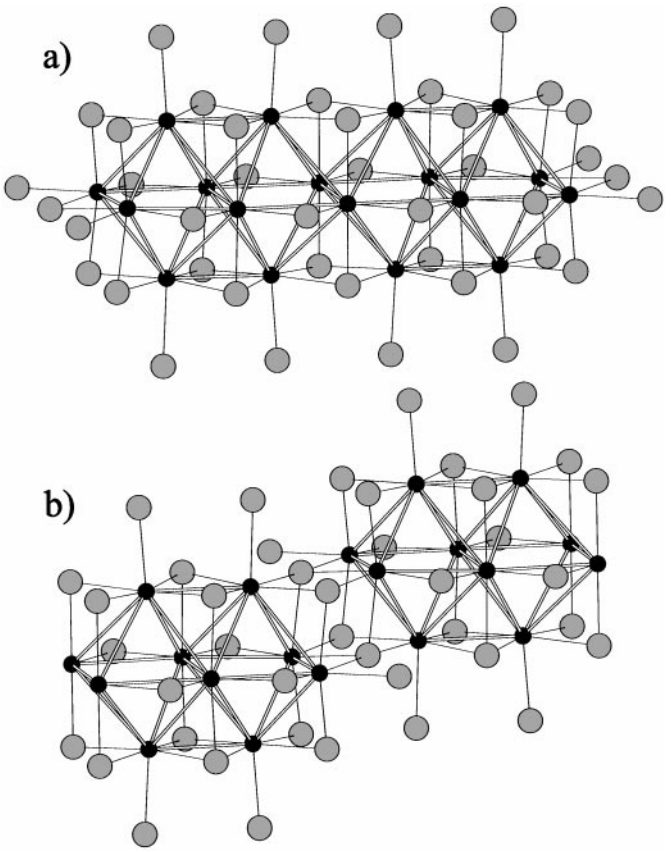

FIG. 1. (a) Structural representation of an individual $Mo_{4n+2}O_{8n+10}$ cluster with $n = 4$. Due to interconnection the oxygen content changes to $Mo_{4n+2}O_{6n+4}$ in the respective cluster compounds. Part of this interconnection, the connection of cluster ends, is depicted in (b). Solid circles denote Mo, shaded circles O.

molybdenum octahedra. Lii *et al.* (5) found the shortest *inter*octahedron Mo–Mo distance with 272.7 pm, however, to be shorter than some of the *intra*octahedron ones with 286.1 or 285.6 pm. Relying on bond length–bond strength considerations it must be concluded that no monomeric Mo_6O_{18} clusters are present in $BaMo_6O_{10}$, and the member with $n = 1$ is still missing in the reduced molybdenum oxide cluster series $M_{n\pm\delta}Mo_{4n+2}O_{6n+4}$. Nevertheless, clusters as well as the related cluster compounds with $n \neq 1$ are often designated as oligomeric, and those with $n \to \infty$ as polymeric.

Two detailed studies by HREM have been recently devoted to $In_5Mo_{18}O_{28}$ (9, 11) and the $Sn_xMo_{10}O_{16}$–$Sn_yMo_{14}O_{22}$ system (12). It has been shown that—among others—polytypism, intergrowth of different polytypes, stacking disorder, ordered and disordered chemical intergrowth of different oligomeric clusters, as well as polysynthetic twinning on a microscopic scale are real-structure phenomena that must be expected when preparing compounds of this family and investigating them by X-ray methods. $Ba_3Mo_{18}O_{28}$ was found to crystallize in space group $P2_1/a$; cell parameters were precisely determined and the structure successfully solved and refined (3). Some minor problems remained with respect to the violation of systematic absences in the X-ray diffraction patterns, faint residual electron densities in the difference map after final refinement, some anomalous temperature factors for the oxygen atoms, and the possible ordering of the three barium atoms on their four countercation sites. It seemed therefore a useful task to investigate $Ba_3Mo_{18}O_{28}$ by HREM. Moreover, it was expected that this compound would not undergo the electron-beam induced phase transformation, which made HREM of the indium and tin oxomolybdates somewhat delicate.

Forthcoming papers (Parts II and III) will be dedicated to the real structure of $K_{0.19}Ba_{3.81}Mo_{22}O_{34}$, a compound which is closely related to the one treated in the present paper (Part I)—but offering even more plentiful defect phenomena.

EXPERIMENTAL

A few small crystals were selected from the $Ba_3Mo_{18}O_{28}$ powder synthesized by Schimek *et al.* (3) and finely crushed in an agate mortar and then suspended in *n*–butanol and fixed on a holey carbon film. Investigations by HREM, selected–area electron diffraction (SAD), and electron probe microanalysis (EPMA) were performed with a PHILIPS CM30 electron microscope equipped with a SuperTWIN lens and a LaB_6 cathode. Operating at 300 kV the point resolution is 0.19 nm. Using 2.3-mm grids and the respective specimen holder a maximum tilt of $\pm 25^\circ$ was possible in two directions. Defocus series, i.e., series of images at different defocus values Δf, were taken whenever the positional stability of the specimens allowed it. SAD patterns were taken using a selected area diaphragm which made the diffraction information originate from a specimen region 250 nm in diameter. Complementary EPMA by energy dispersive X-ray spectroscopy (EDXS) was carried out using a NORAN HP-Ge detector with ultrathin window and a Voyager-I system.

The EMS program package (13) was used for the simulation of HREM images with exit-wave functions calculated according to the multislice formalism. The spherical aberration constant C_S amounted to 1.15 mm, the defocus spread parameter was $\Delta = 7$ nm, and the illumination semiangle was determined to be $\alpha = 1.2$ mrad. The simulation of kinematical electron diffraction (ED) patterns was carried out with a program based on the source PATTERN (14). For some diffracted beams of particular interest, dynamical intensities (as a function of crystal thickness) were calculated with the multislice routine of EMS (13).

HREM images and SAD patterns were partly registered on photographic material and partly with a GATAN

Slow-Scan CCD Camera 694 (1024×1024 pixels). In order to reduce the influence of amorphous surface layers sometimes existing on the investigated crystal fragments, all the HREM images reproduced in this paper were Fourier filtered (GATAN Digital–Micrograph software) applying a band-pass mask.

RESULTS AND DISCUSSION

The lattice parameters of $Ba_3Mo_{18}O_{28}$–1*M*, as determined by Schimek *et al.* (3), are $a = 0.9939$ nm, $b = 0.9377$ nm, $c = 1.3057$ nm, and $\beta = 100.92°$. The structure is denoted by the Ramsdell symbol 1*M* (15), since it will turn out that there is another ordered polytype besides the monoclinic one. Figure 2a illustrates the parallel projections of the crystal structure along [0 1 0], [1 1 0], and [1 0 0]. The Mo octahedra situated at the cluster ends and the Ba sites coordinating them are hereafter denoted as *outer* and the remainder as *inner* ones.

It is a common feature of all the known monoclinic representatives of the the family $M_{n\pm\delta}Mo_{4n+2}O_{6n+4}$, which crystallize in $P2_1/a$, that every cluster layer is shifted by nearly exactly **a**/4 with respect to its preceding layer. For $Ba_3Mo_{18}O_{28}$–1*M* the error $(4 \cdot c \cdot \cos(180° - \beta) - a)/a$ is only -0.45%. Hence, every fifth layer projects nearly exactly onto the first, when viewing along the cluster axes, which are almost parallel to [1 0 4]. Based upon this approximation, the stacking sequence may be denoted as *ABCDA*.

There are two favorable crystal orientations, [0 1 0] and [1 1 0], in $Ba_3Mo_{18}O_{28}$ as well as in all the other known members of the family $M_{n\pm\delta}Mo_{4n+2}O_{6n+4}$ (cf. (9)), with indexing of the lattices referred to the nonstandard space group settings $P2_1/a$, *Pnam*, and $P2_1am$, respectively. The oligomeric clusters themselves can be imaged most instructively in [0 1 0] orientation, but then information on the monoclinic stacking sequence is widely lost. If the monoclinic cell had not been drawn in the [0 1 0] projection of Fig. 2a, the structure would appear to be orthorhombic. The monoclinic symmetry becomes discernible only by precise measurement of angles and careful inspection of details in the representation. It is especially noteworthy that, in the [0 1 0] projection, the Ba cations are behind or in front of the the *trans* edge-shared Mo octahedra. On the other hand, the *ABCDA* stacking can be derived directly from the [1 1 0] projection, and it becomes immediately evident that every fifth cluster layer projects nearly exactly onto the first. In experimental HREM micrographs taken in [1 1 0] orientation, however, the number *n* of *trans* edge-sharing molybdenum octahedra in the cluster can be identified only via metrics or by comparison with computer simulated images. HREM imaging in [1 0 0] orientation is less instructive. The stacking sequence cannot be visualized, nor can the cluster length *n* be discerned easily.

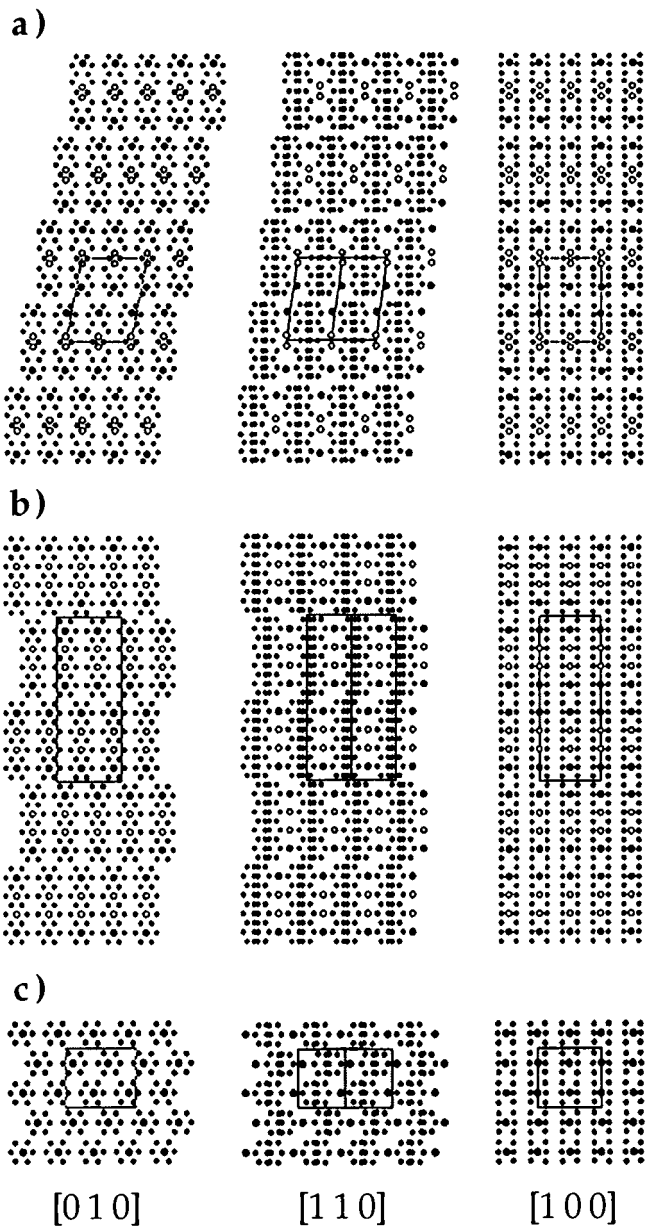

FIG. 2. The structures of (a) $Ba_3Mo_{18}O_{28}$–1*M*(3), (b) $Ba_3Mo_{18}O_{28}$–2*O* (see Table 1), and (c) orthorhombic $BaMo_6O_{10}$ (5) projected along [0 1 0], [1 1 0], and [1 0 0] zone axes with the unit cells indicated. Small solid circles denote Mo, large open circles partially occupied Ba sites, large solid circles fully occupied Ba sites; O is omitted for clarity. As displayed in the [1 1 0] orientation, the stacking sequence are (a) *ABCDA* and (b, c) *ABABA*.

SAD patterns for different orientations of $Ba_3Mo_{18}O_{28}$–1*M* are shown in Fig. 3, together with kinematical ED patterns simulated using the single-crystal X-ray data by Schimek *et al.* (3). Discrepancies between experimental and simulated ED patterns are readily apparent for the [1 1 0] orientation; they are small for [0 1 0] and nearly nonexistent for [1 0 0]. In the case of [1 1 0] and [0 1 0] they concern

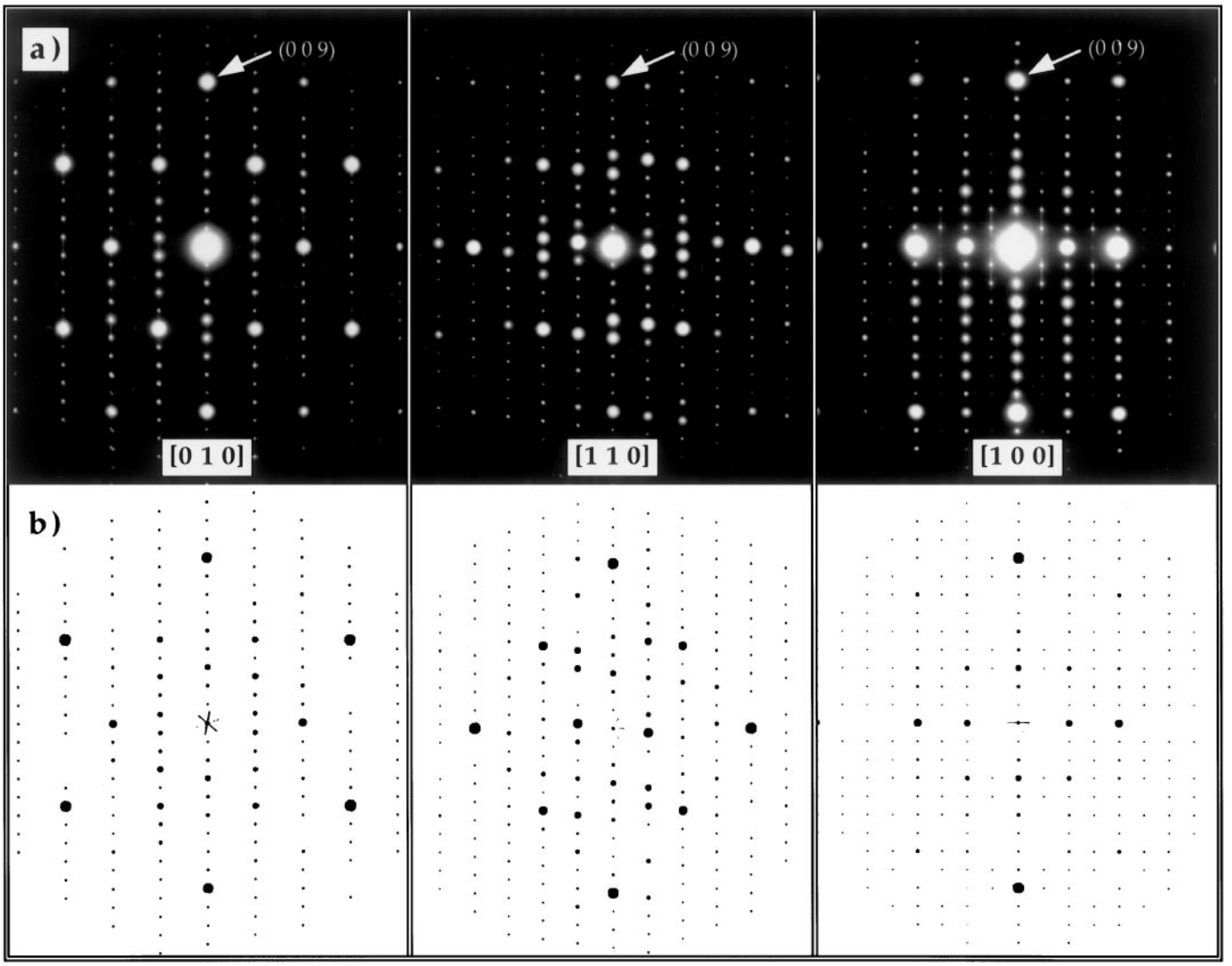

FIG. 3. (a) SAD patterns of $Ba_3Mo_{18}O_{28}$–1*M* for the [0 1 0], [1 1 0], and [1 0 0] orientations, together with (b) kinematical ED patterns simulated on the basis of X-ray data (3).

mainly the row of (0 0 *l*) reflections: Whereas (0 0 3) is stronger than all (0 0 *l*) with $0 < l < 9$ in the simulations, the pair (0 0 4) and (0 0 5) is stronger in the experimental results. These discrepancies may be due to either dynamical diffraction effects or incorrect X-ray data.

In order to decide between both possibilities dynamical multibeam diffraction intensities have been calculated as a function of crystal thickness for prominent reflections. In addition, SAD patterns were registered with a slow-scan CCD camera; thus ED intensities could be determined more reliably than by photographic–film registration. It has to be stated that the experimental ED patterns under consideration may be generally understood on the basis of the X-ray data by Schimek *et al.* (3). Effects due to dynamical diffraction are smallest in the [1 0 0] pattern and stronger in the [1 1 0] and [0 1 0] patterns. Small inconsistencies are perhaps to be attributed to defects in the single crystals analyzed by X-ray methods. As will be shown below such defects can never be completely excluded, and they are surely responsible for the minor problems reported by Schimek *et al.* (3) with respect to their X-ray results.

A defocus series of HREM micrographs in [1 1 0] orientation is given in Fig. 4; computer simulated HREM images are inserted. Independently of the defocus value, the stacking sequence *ABCDA* can be derived directly. To identify the oligomeric clusters as tetrameric is, however, difficult. The micrograph in Fig. 4e, which shows rows of four white dots, provides the impression of four-membered units best, but there is a remarkable discrepancy with the simulated image. This discrepancy concerns the intensity of the two

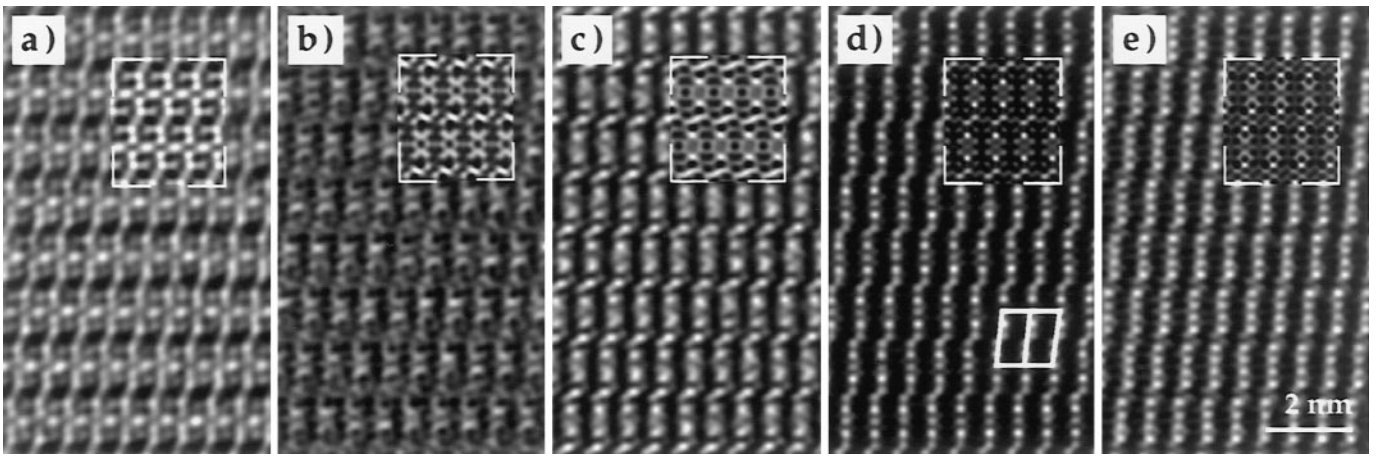

FIG. 4. HREM images of $Ba_3Mo_{18}O_{28}$–1*M* in the [1 1 0] orientation imaged with different defocus values. The stacking sequence is *ABCDA* (unit cell indicated). Computer simulated images are shown as insets. Specimen thickness $t = 4.1$ nm; (a) $\Delta f = +20$ nm, (b) $\Delta f = -30$ nm, (c) $\Delta f = -45$ nm, (d) $\Delta f = -60$ nm, and (e) $\Delta f = -80$ nm.

inner white dots, which are only slightly weaker than the two outer ones in the experimental image, whereas they are markedly weaker in the simulated image. Only for the defocus value of Fig. 4e is agreement between the experimental and the simulated image missing; for all the other images in the defocus series agreement is good. Minor deviations are due to the very small specimen thickness, which makes it unlikely that the statistical 50% occupancy of the inner countercation positions is reflected in the HREM image. It seems worth mentioning that the experimental image of Fig. 4e cannot be simulated for any value of defocus and specimen thickness. Since image simulation (13) is well established and very reliable, this is another hint of the slight incorrectness of the X-ray data (3) used.

Figure 5 shows HREM images of a rather thin specimen in [0 1 0] orientation for two different defocus values, again with computer simulations inserted. Figure 5b was taken near to the Scherzer optimum defocus ($\Delta f_{\text{Scherzer}} = -60$ nm). Consequently, if the specimen is very thin and the weak phase-object approximation holds, the HREM image can be interpreted straightforwardly: Heavier atoms and clusters thereof are imaged in black, whereas the spaces in between are imaged in white. Figure 5b can be likened to elongated honeycombs which are composed of four black hexagons corresponding to the projection of four Mo octahedra. It should be stressed that—with Scherzer defocus and with a very thin specimen—a microscope with a point resolution better than 0.14 nm would be needed to resolve the single Mo atoms of the octahedra. The bright spots surrounding each elongated honeycomb represent spaces between Mo cluster cores which are filled with oxygen atoms. The less bright spots in the interior of each black hexagon represent a view through the Mo octahedra onto the Ba countercation positions (cf. the structure projected along [0 1 0] in Fig. 2a). The two outer countercation positions are fully occupied and the white spots are only faint; the two inner positions are occupied by 50% and the corresponding white spots are less faint. A completely different contrast situation is met in Fig. 5a. Now the positions of the Ba countercations are highlighted. The brighter, diffuse white spots represent the fully occupied outer countercation positions, whereas two less bright, diffusely streaked white

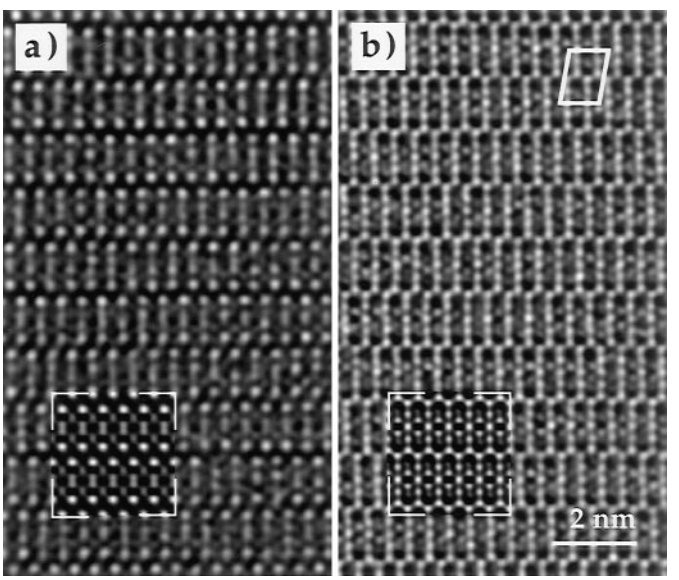

FIG. 5. HREM images of $Ba_3Mo_{18}O_{28}$–1*M* in the [0 1 0] orientation (unit cell indicated) imaged with two different defocus values. Computer simulated images are shown as insets. (a) $\Delta f = +10$ nm highlights the countercation positions, (b) $\Delta f = -50$ nm highlights the "channels" in the projected structure; specimen thickness $t = 4.7$ nm.

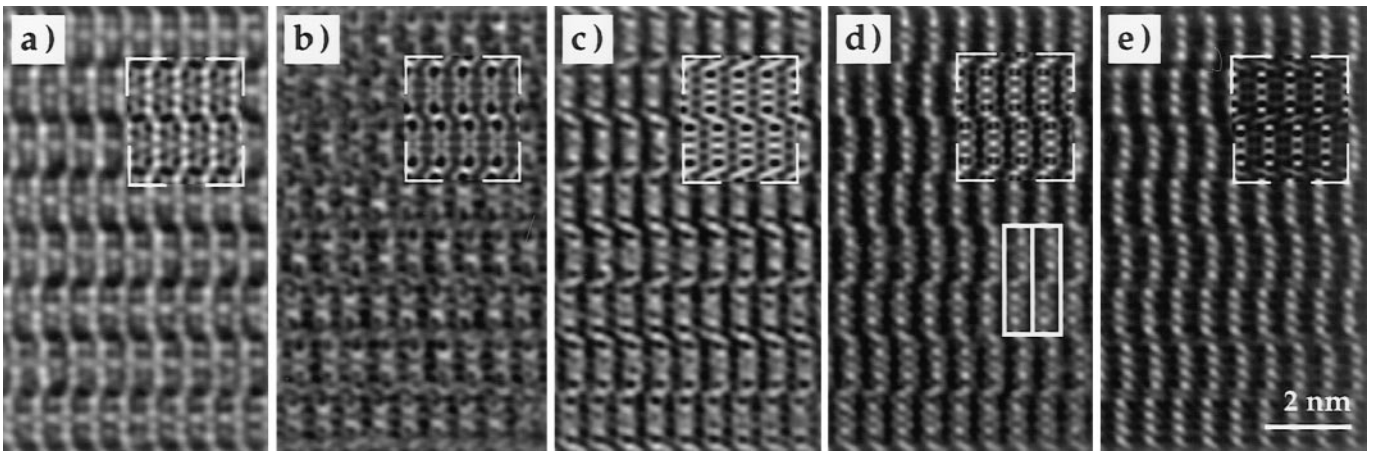

FIG. 6. $Ba_3Mo_{18}O_{28}$–2*O* in the [1 1 0] orientation imaged at the same specimen thickness and with the same defocus values as applied for the 1*M* modification in Fig. 4. The stacking sequence is *ABABA* (unit cell indicated). Computer simulated images are shown as insets. Specimen thickness $t = 4.1$ nm; (a) $\Delta f = +20$ nm, (b) $\Delta f = -30$ nm, (c) $\Delta f = -45$ nm, (d) $\Delta f = -60$ nm, and (e) $\Delta f = -80$ nm.

spots represent the partly occupied inner positions. Consequently, there is a chemically sensitive defocus, which can be used to extract valuable information about the Ba countercations accompanying each cluster. In those regions of the specimen which are thick enough to integrate (along the direction of projection) over a sufficient number of unit cells, the HREM image corresponds to the statistical distribution of Ba countercations on the two inner positions. There is no indication on any countercation ordering. Of course, in the thinnest regions of the specimen the HREM images must not necessarily reflect the statistical distribution of Ba on the partly occupied inner positions. In Fig. 5a one of the inner white spots is sometimes as bright or nearly as bright as the two outer ones, the other of the inner spots being then almost invisible. The occupancy of countercation positions in the respective columns, which are perhaps only a few unit cells thick, cannot then be statistically equalized.

In the course of our HREM investigatons it proved that $Ba_3Mo_{18}O_{28}$ exists, at least, in two ordered polytypes (modifications). Fig. 6 shows a defocus series which is completely analogous to the one in Fig. 4, except that the stacking sequence is not *ABCDA* but *ABABA*. The latter sequence is characteristic of those representatives of the family $M_{n\pm\delta}Mo_{4n+2}O_{6n+4}$, which crystallize in space groups *Pnam* and $P2_1am$. The lattice parameters of the new polytype, $Ba_3Mo_{18}O_{28}$–2*O*, can be derived from those of $Ba_3Mo_{18}O_{28}$–1*M* as $a \approx 1.00$ nm, $b \approx 0.94$ nm, and $c \approx 2.56$ nm. The crystal orientation in Fig. 6 is then [1 1 0]. It should be noted that the cluster layers in both ordered polytypes appear absolutely identical over the whole range of defocus values, except for faint differences caused by the different interconnections of layers—*trans* or *cis*. Other contrast differences, recocnizable best in Figs. 4b and 6b, are due to statistical distribution of Ba on the two inner countercation sites. HREM images of $Ba_3Mo_{18}O_{28}$–2*O* in [0 1 0] orientation are shown in Fig. 7. The 2*O* polytype exists most frequently in rather small domains intergrown with the 1*M* polytype, which constitutes the majority ($\approx$ 70%) of the investigated material. In rare cases entire microcrystallites consist of $Ba_3Mo_{18}O_{28}$–2*O*. Such microcrystallites could be analyzed by EDXS, and the SAD patterns of Fig. 8 could be taken. There is no evidence in the EDXS results for any difference in the Ba/Mo ratio between

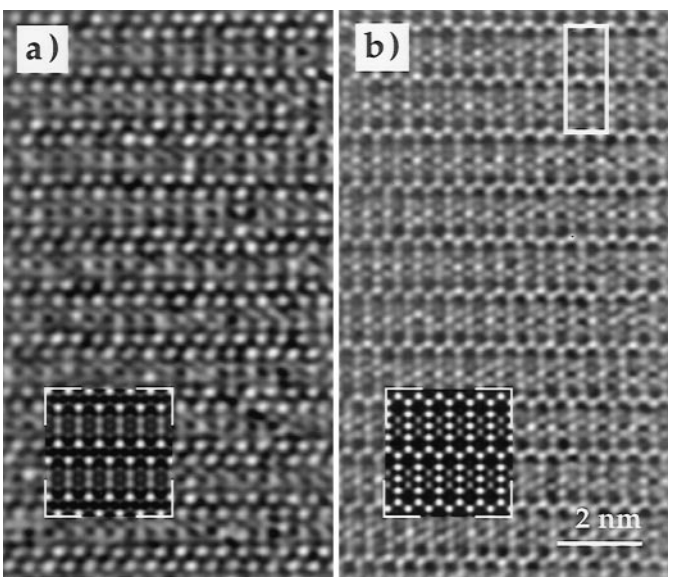

FIG. 7. $Ba_3Mo_{18}O_{28}$–2*O* in the [0 1 0] orientation (unit cell indicated) imaged at the same specimen thickness and with the same defocus values as applied for the 1*M* modification in Fig. 5. Computer simulated images are shown as insets. Specimen thickness $t = 4.7$ nm; (a) $\Delta f = +10$ nm, (b) $\Delta f = -50$ nm.

the two polytypes. A quantitative determination of the oxygen content in both polytypes could not be performed reliably.

The HREM images of Fig. 7 should be compared with those in Fig. 5, which shows the analogous projection for the 1*M* polytype. As expected, differences cannot be perceived. The 2*O* polytype shows no indication of Ba ordering, either. Precise measurement of angles in the images could reveal that the projected structure in Fig. 7 is rectangular whereas that in Fig. 5 is only pseudorectangular. Since the deviations are very small, it appeared more practicable to identify the polytypes shown in Figs. 5 and 7 via the Fourier transform of the respective HREM images or, if domains are large enough, by SAD.

Since structural data for the 2*O* modification are not yet available, an idealized set of atomic coordinates was generated under the assumption that the tetrameric clusters are built from ideal, rigid Mo octahedra, that the Ba countercations are arranged on a straight line with a constant Ba–Ba distance of 284.3 pm, and that oxygen atoms can be completely neglected Table 1. Figure 2b illustrates the parallel projections of the idealized 2*O* structure in [0 1 0], [1 1 0], and [1 0 0] directions. The generated set of data was used to simulate the HREM images of Figs. 6 and 7. In [0 1 0] orientation (Fig. 7) the agreement between experimental and simulated images is satisfactory and comparable to the 1*M* modification (Fig. 5). In [1 1 0] orientation (Fig. 6) agreement is not as good in details compared with most of the defocus values for the 1*M* modification (Fig. 4). This may be attributed to the exclusion of oxygen atoms in the 2*O* structure model. However, the HREM image for $\Delta f = -80$ nm (cf. Figs. 4e and 6e) is now simulated much closer. Comparison between the projected structures and computer simulated images shows that, with this particular defocus, the positions of Ba countercations are highlighted, and it may be speculated that the coordinates of the partly occupied Ba positions are more realistic in the idealized set of data for the 2*O* polytype (Table 1) than in the X-ray data for the 1*M* polytype (3).

TABLE 1
Idealized Atomic Coordinates for $Ba_3Mo_{18}O_{28}$–2*O*

Atom	Wyckoff position	*X*	*Y*	*Z*
Mo1	4*e*	0.0403	0.1231	0.0834
Mo2	4*e*	0.0403	0.1231	0.1945
Mo3	4*e*	0.4576	0.6230	0.0279
Mo4	4*e*	0.2924	0.3769	0.0279
Mo5	4*e*	0.2097	0.6230	0.0834
Mo6	4*e*	0.4576	0.6230	0.1390
Mo7	4*e*	0.2924	0.3769	0.1390
Mo8	4*e*	0.2097	0.6230	0.1945
Mo9	4*c*	0.4576	0.6230	0.2500
Mo10	4*c*	0.2924	0.3769	0.2500
Ba1	4*e*	0.3750	0.0000	0.0834
Ba2[a]	4*e*	0.3750	0.0000	0.1945

[a] Site occupancy for Ba2 is 50%.

A supposition formulated earlier (9), that polytypism is common to all the representatives of the series $M_{n\pm\delta}Mo_{4n+2}O_{6n+4}$ with $n \geq 4$, has been confirmed once more. In Part II of this study it will be discussed in detail why polytypism in this class of materials was always overlooked in the original X-ray studies and first observed by HREM. Most probably the 2*O* polytype crystallizes in space group *Pnam*, as—according to X-ray single-crystal analysis—do $In_6Mo_{22}O_{34}$–2*O* (16) and $In_5Mo_{18}O_{28}$–2*O* (17). There is no indication in the HREM images for the inversion symmetry being violated. Like in the 1*M* polytype

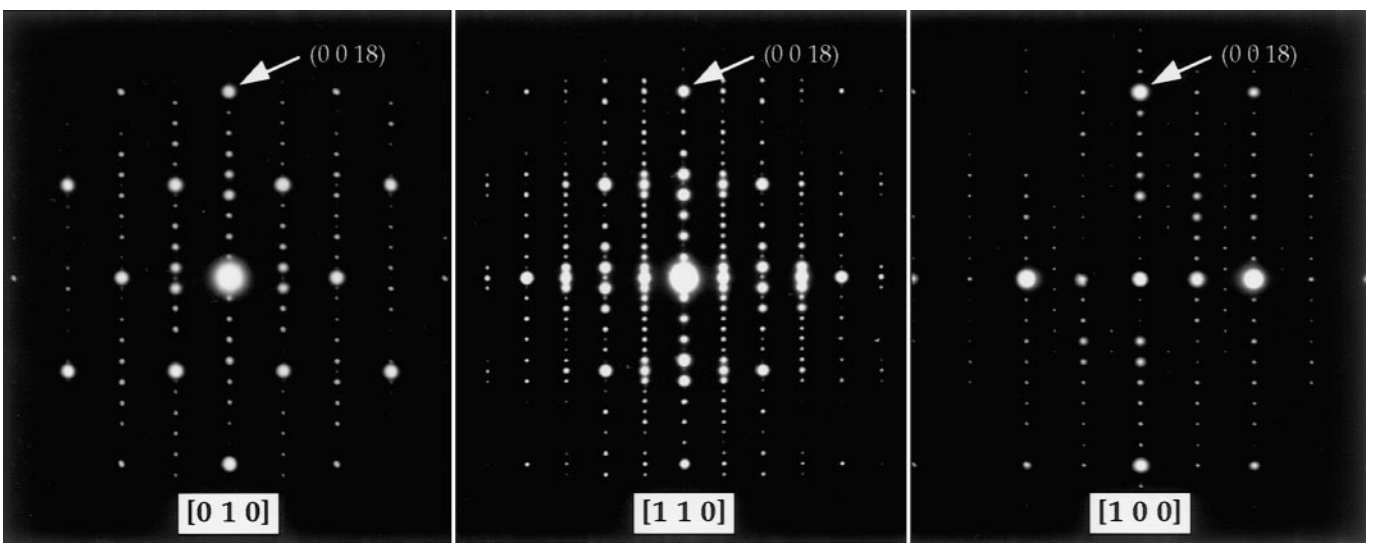

FIG. 8. SAD patterns of $Ba_3Mo_{18}O_{28}$–2*O* for the [0 1 0], [1 1 0], and [1 1 0] orientations.

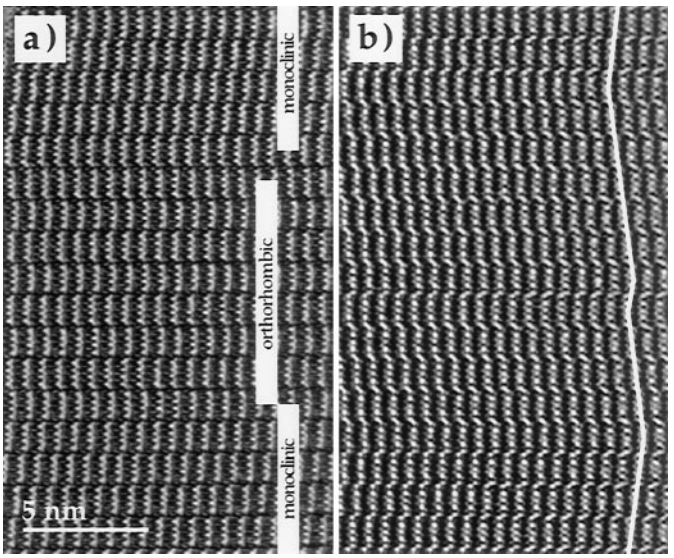

FIG. 9. HREM images in the [1 1 0] orientation of (a) monoclinic and orthorhombic domains (indicated) of $Ba_3Mo_{18}O_{28}$ intergrown with each other and (b) polysynthetic microtwinning (slope indicated) of $Ba_3Mo_{18}O_{28}$–1*M* through the (0 0 1) plane. Stacking sequence may be easily realized!

the two outer Ba sites seem to be equally and fully occupied, whereas the third Ba cation is statistically distributed over the two inner sites. In either polytype, 1*M* or 2*O*, there is no indication of any Ba cation ordering, and it remains still unknown why polytypism occurs at all. It would be a creditable attempt to grow single crystals of the 2*O* modification (or isolate them from the crystalline powder) which are large enough for X-ray single-crystal analysis. The idealized set of data for $Ba_3Mo_{18}O_{28}$–2*O* (with oxygen atoms excluded) presented in Table 1 is only meant to computer simulate the general features of HREM images.

Often the lamellar domains of 1*M* and 2*O* are only a few cluster layers thick, and it would be more adequate to speak of stacking disorder instead of two ordered polytypes intergrown with each other (Fig. 9a). Another frequently observed phenomenon is polysynthetic twinning of $Ba_3Mo_{18}O_{28}$–1*M* through the (0 0 1) plane, with the twin domains being microscopically thin (Fig. 9b).

Besides polytypism, stacking disorder, and polysynthetic twinning the chemical intergrowth of a different phase, $BaMo_6O_{10}$, is a typical defect in $Ba_3Mo_{18}O_{28}$. According to Lii *et al.* (5) $BaMo_6O_{10}$, the member with $n = 1$ in the considered series of compounds, crystallizes in *Pnam* with lattice parameters $a = 1.0154$ nm, $b = 0.9184$ nm, and $c = 0.8641$ nm. Projections of its crystal structure are shown in Fig. 2c. The *a* and *b* lattice parameters of $BaMo_6O_{10}$ are very close to those parameters of $Ba_3Mo_{18}O_{28}$–1*M*. The misfit is $+2.2\%$ along the *a*-axis and -2.1% along the *b*-axis. That means that the misfits can be completely compensated by small distortions in the *a*–*b* plane. The same conclusion can be drawn for $BaMo_6O_{10}$ intergrown with $Ba_3Mo_{18}O_{28}$–2*O*. HREM images of $BaMo_6O_{10}$ intergrown in $Ba_3Mo_{18}O_{28}$ are given in Figs. 10a and 10b. Both matrix and intergrowth lamellae are in [0 1 0] orientation; a computer simulated image of the $BaMo_6O_{10}$ is inserted.

Other, however less typical, defects in $Ba_3Mo_{18}O_{28}$ are intergrown monolayers of dimeric, trimeric, and pentameric clusters. The latter are well known in the related compound $K_{0.19}Ba_{3.81}Mo_{22}O_{34}$, but now it is most probably

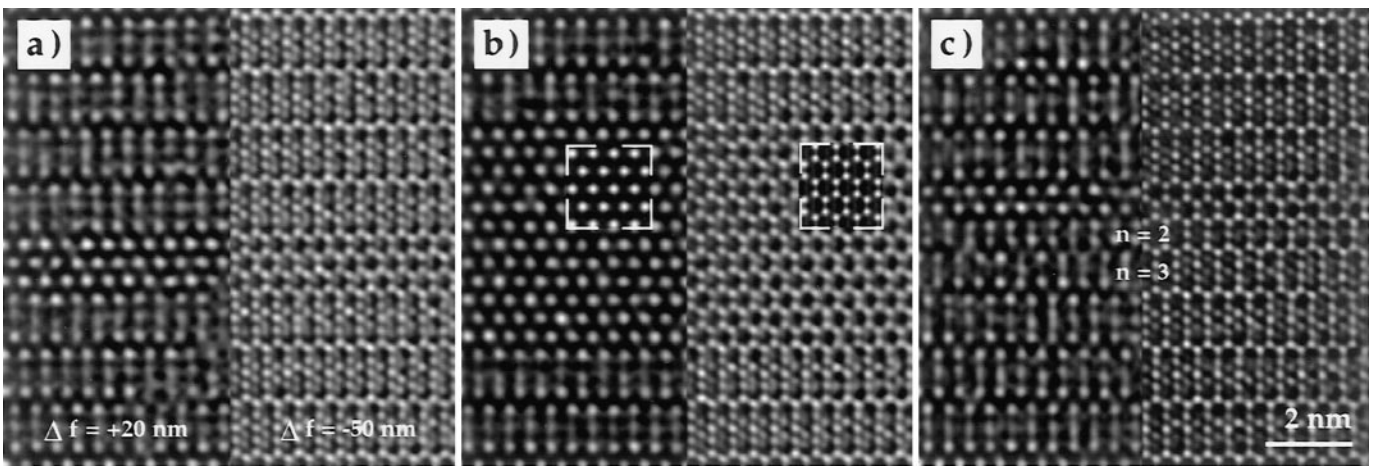

FIG. 10. Chemical intergrowth of "monomeric," dimeric, and trimeric clusters in a matrix of $Ba_3Mo_{18}O_{28}$. HREM images in [0 1 0] orientation (specimen thickness $t \approx 5$ nm) were taken with two different defocus values: $\Delta f = +20$ nm (left) highlights the Ba cation positions and $\Delta f = -50$ nm (right) highlights the channels in the projected structure; i.e., clusters are imaged in black. (a) Lamella of $BaMo_6O_{10}$ 3 layers of "monomeric clusters" thick and (b) lamella of $BaMo_6O_{10}$ 12 layers of "monomeric clusters" thick. Images computer simulated on the basis of X-ray data (5) are shown as insets in (b). (c) Lamella comprising layers of "monomeric," dimeric (indicated), and trimeric (indicated) clusters.

accompanied by four Ba countercations. Compounds with dimeric and trimeric clusters are not yet known in the $M_{n\pm\delta}Mo_{4n+2}O_{6n+4}$ series with $M = Ba$. The HREM images in Fig. 10c allow conclusions concerning the distribution of Ba countercations. In the case of the dimeric clusters ($n = 2$), the two possible countercation sites are equally occupied. Most probably they are even fully occupied, since there is no deviation from an equal distribution to be observed. The suggested composition of an intergrowth layer consisting of dimeric clusters is $Ba_2Mo_{10}O_{16}$. Then, the electron transfer to the cluster anion would be 4; the same value as formally determined for the compound $Sn_2Mo_{10}O_{16}$ (18). In the case of the trimeric clusters ($n = 3$), it seems that the two outer sites are preferentially and equally occupied and that the central site has a lower occupancy than the outer ones. Contrasts, however, often deviate from the proposed occupancies, since the imaged specimen regions are too thin. The composition of an intergrowth layer of trimeric clusters would then be $Ba_{n-\delta}Mo_{14}O_{22}$ with $2 < n - \delta < 3$. The expected electron transfer to the cluster anion is greater than 4 and smaller than 6. This is a quite reasonable result considering the values formally determined for some compounds containing trimeric clusters: 5.6 electrons for $Tl_{1.6}Sn_{1.2}Mo_{14}O_{22}$ (19); 3 for $K_3Mo_{14}O_{22}$; 4.3 for $K_{1.66}Pb_{1.34}Mo_{14}O_{22}$; and 4.7 for $K_{1.29}Sn_{1.71}Mo_{14}O_{22}$ (20).

Since intergrowth layers of pentameric clusters (not shown in this paper) were found in $Ba_3Mo_{18}O_{28}$, it may be speculated that—besides $K_{0.19}Ba_{3.81}Mo_{22}O_{34}$—$Ba_4Mo_{22}O_{34}$ should also exist as a discrete phase. On the other hand, only monolayers were observed, never multilayers or extended domains. This is perhaps a hint that the pentameric cluster is not stabilized sufficiently when accompanied by four Ba cations.

As shown in Figs. 10a and 10b, $BaMo_6O_{10}$ lamellae are often three cluster layers thick—or simple multiples thereof. It is noticed that a single layer of tetrameric clusters in $Ba_3Mo_{18}O_{28}$, both $1M$ and $2O$, is approximately 1.28 nm thick, whereas three layers of "monomeric clusters" (in $BaMo_6O_{10}$) are $3/2 \cdot c = 1.2962$ nm thick. The small misfit of $+1.3\%$ along the direction perpendicular to the a–b plane would, however, be meaningless if the lamellae of intergrowth layers were always infinite in their lateral dimension. Indeed, it proved that intergrowth lamellae can also laterally border on matrix layers. This phenomenon is illustrated in Fig. 11. A matrix layer of tetrameric clusters "dissociates" into three intergrowth layers of monomeric clusters. The structure of the resultant defect, which is located in the center of Figs. 11a and 11b, is schematically given in Fig. 11c. The dissociating layer of tetrameric clusters is terminated by irregularly condensed five-membered clusters. They are characterized by a fifth Mo octahedron which is *cis*-edge condensed to the second and third member of the four *trans*-edge condensed Mo octahedra, thus forming a T-shaped building unit. The suggested defect enables the boundary between the one layer of tetrameric clusters and the three intergrowth layers of monomeric clusters to be—in a general sense—highly coherent, in particular, to be free of voids. An irregular cluster condensation like the one suggested here, has recently been found when investigating twin boundaries in a related compound by HREM (21).

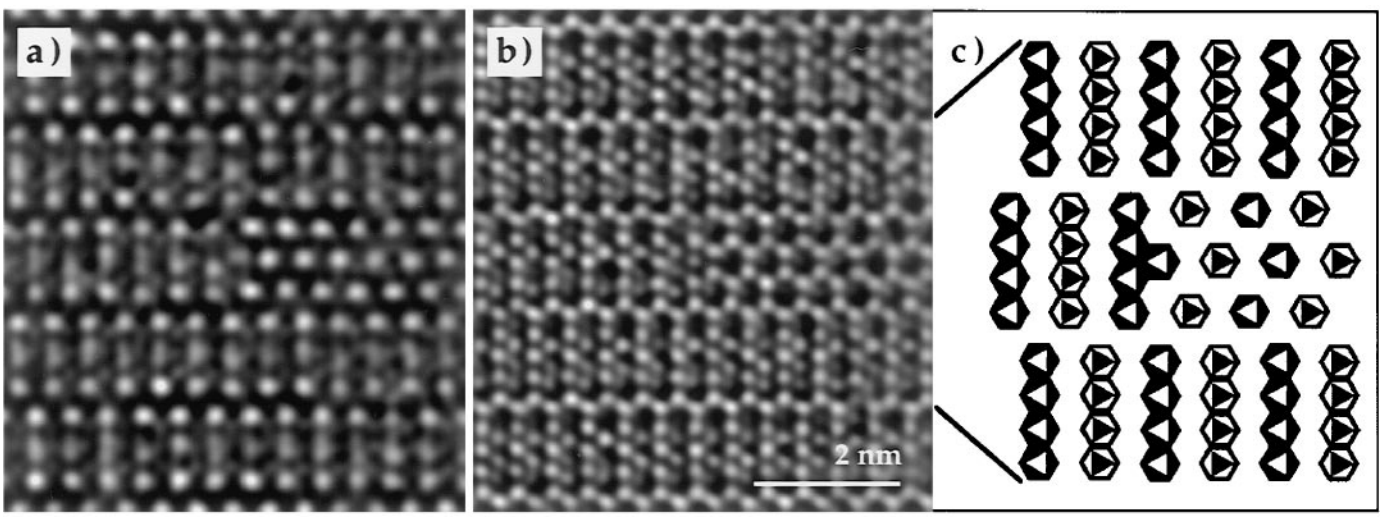

FIG. 11. Dissociation of one layer of *cis* connected tetrameric clusters in three layers of "monomeric" clusters. HREM images in [0 1 0] orientation (specimen thickness $t \approx 5$ nm) were taken with two different defocus values: (a) $\Delta f = +20$ nm and (b) $\Delta f = -50$ nm. At the end of the dissociating layer irregularly condensed pentameric clusters are formed. The defect is schematically illustrated in (c). Different contrasts for the projected Mo octahedra mean different positions along the b-axis, $Y = 0.0$ or $Y = 0.5$.

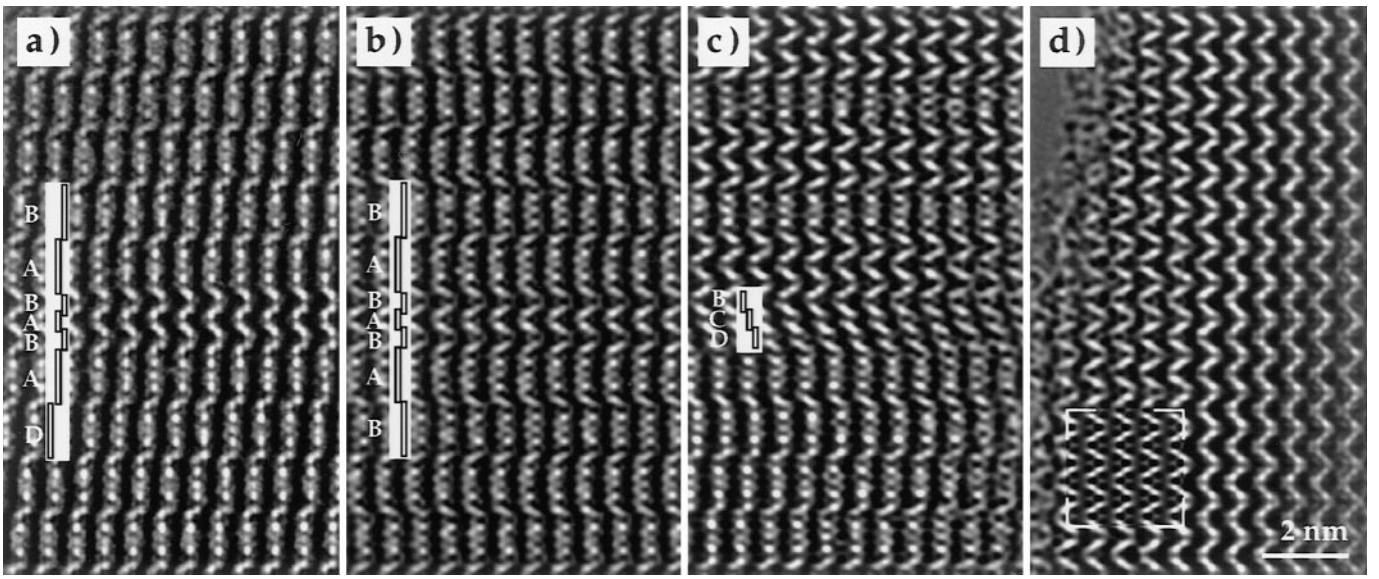

FIG. 12. HREM images in [1 1 0] orientation of intergrown $BaMo_6O_{10}$ in a matrix of $Ba_3Mo_{18}O_{28}$. The stacking sequences are indicated (a–c). Three layers of orthorhombically stacked "monomeric clusters" are imaged in (a) $Ba_3Mo_{18}O_{28}$–1*M* and (b) $Ba_3Mo_{18}O_{28}$–2*O*. In both cases the intergrowth lamella imposes its *cis* connection on the adjacent matrix layers. Another region is imaged in (c). Among the various intergrowth lamellae, all three "monomeric cluster" layers thick, is one with a monoclinic stacking sequence. (d) large domain of orthorhombic $BaMo_6O_{10}$. The stacking sequence is *ABABA*. The inset shows an image computer simulated on the basis of X-ray data (5). Specimen thickness $t = 4.1$ nm; $\Delta f = -50$ nm.

HREM images with both matrix and intergrowth lamellae in [1 1 0] orientation are shown in Figs. 12a and 12b. They prove that $BaMo_6O_{10}$ intergrowth lamellae occur both in the 1*M* and the 2*O* modifications of $Ba_3Mo_{18}O_{28}$, with the intergrown $BaMo_6O_{10}$ layers almost always following the orthorhombic *ABABA* stacking sequence, which is expected from the structure reported by Lii *et al.* (5). In the case of a 1*M* matrix, the orthorhombic stacking of the intergrowth layers is imposed on—at least—the top and bottom adjacent matrix layers. Assuming the number of intergrowth layers to be 3, the resultant stacking sequence is: *ABCDA*/*BAB*/*A*BCDA. In the case of a 2*O* matrix, the orthorhombic stacking of the intergrowth layers is always in step with the stacking of the matrix layers: *ABABA*/*BAB*/*A*BABA. This behavior indicates a strong tendency of the monomeric cluster to be *cis* connected. There are, however, infrequent exceptions. As shown in Fig. 12c, intergrowth lamellae of $BaMo_6O_{10}$, three layers thick, have also been observed with a monoclinic stacking sequence. Pure $BaMo_6O_{10}$ should be prepared and investigated by HREM to give more evidence for this result. One might postulate, nevertheless, that $BaMo_6O_{10}$ also exists in two polytypic modifications. It is not easy to recognize that the intergrowth lamellae in Figs. 12a and 12b are really of (orthorhombic) $BaMo_6O_{10}$. In Fig. 12d a large domain of $BaMo_6O_{10}$ in [1 1 0] orientation is shown for comparison. Having understood the contrast in the case of orthorhombic stacking, it becomes obvious that monoclinic stacking occurs in Fig. 12c.

The frequent intergrowth of $BaMo_6O_{10}$ ($\equiv Ba_3Mo_{18}O_{30}$) in both modifications of $Ba_3Mo_{18}O_{28}$ is not a surprising observation in view of the very small difference in the oxygen content of both compounds, 58.8 and 57.1 at.%, respectively. One must be aware that this intergrowth can hardly be avoided when preparing $Ba_3Mo_{18}O_{28}$ single crystals. Apart from stacking disorder and chemical intergrowth of oligomeric $Mo_{4n+2}O_{8n+10}$ clusters with $n = 2$, 3, and 5, there is hence another serious reason for recognizing that structure data by X-ray single-crystal analysis is a little bit unsure. Moreover, the availability of a very small building unit, i.e. the "monomeric cluster," facilitates the occurrence of other defects as twin boundaries, generalized dislocations (dissociation of cluster layers), and irregular cluster condensation. Exactly this abundance of defect structures, in combination with the compound's strong resistance to electron beam damage, makes $Ba_3Mo_{18}O_{28}$ an excellent material for studying such extended defects in cluster compounds.

CONCLUSIONS

$Ba_3Mo_{18}O_{28}$ exists in two ordered polytypes, 1*M* and 2*O*. The second polytype was discovered by HREM. It crystallizes most probably in space group *Pnam* with approximate lattice parameters: $a \approx 1.00$ nm, $b \approx 0.94$ nm,

$c \approx 2.56$ nm. An idealized structure model was generated as a basis for computer simulations of HREM images. X-ray data for the 2*O* modification are not available, but it is suggested that the two modifications differ only in their stacking sequence, as was confirmed by Fais *et al.* (17) for $In_5Mo_{18}O_{28}$, 1*M* and 2*O*. There is no indication in the HREM images of ordering of the three Ba countercations on their four possible sites, in either polytype. HREM images and dynamical SAD patterns of the 1*M* modification could be rather successfully computer simulated with the X-ray data by Schimek *et al.* (3). Small inconsistencies are due to the fact that single crystals used for X-ray analysis were most probably rich in structure defects.

The real structure of the investigated crystals is characterized by both polytypes intergrown with each other, whereby the 1*M* polytype constitutes about 70% of the material. Sometimes ordered domains extend to some micrometers; sometimes they are only three cluster layers thick. The latter case is better described as stacking disorder than chemical intergrowth of ordered polytypes. Like the other reduced oxomolybdates crystallizing in space group $P2_1/a$ (9, 12), the 1*M* modification shows a strong tendency to polysynthetic microtwinning through the (0 0 1) plane.

Another real–structure phenomenon in $Ba_3Mo_{18}O_{28}$ crystals is chemical intergrowth of $Mo_{4n+2}O_{8n+10}$ cluster layers with $n = 2, 3, 5$. Hints on the number of Ba countercations accompanying these oligomeric clusters as well as on the occupancy of their sites were deduced from HREM images. The spectrum of intergrown oligomeric clusters and the frequency of their occurrence is, however, by far smaller than in the related compound $K_{0.19}Ba_{3.81}Mo_{22}O_{34}$, which will be treated in a forthcoming paper (Part III of this study). It may be concluded that in the system *M*–Mo–O with mixed countercations *M*, monovalent K and divalent Ba, a broader spectrum of oligomeric clusters can be sufficiently stabilized than in the system with Ba as the only counter-cation.

Much more often than intergrowth of oligomeric clusters, intergrowth of the phase $BaMo_6O_{10}$ (formally: monomeric clusters, $n = 1$) was observed in both polytypes of $Ba_3Mo_{18}O_{28}$. Intergrowth lamellae ranged from one cluster layer thick to very extended. Because of the similar chemical constitution, it may be an unsolvable problem to avoid this kind of defect when growing $Ba_3Mo_{18}O_{28}$ single crystals. Intergrowth layers of $BaMo_6O_{10}$ impose their orthorhombic stacking sequence to adjacent $Ba_3Mo_{18}O_{28}$ layers, irrespective whether they belong to a 1*M* or a 2*O* domain. That means that the "monomeric" cluster prefers being *cis* connected. In very exceptional cases a monoclinic stacking sequence was observed inside $BaMo_6O_{10}$ intergrowth lamellae, which extends over a few cluster layers. It is therefore regarded possible that also $BaMo_6O_{10}$ is subject to polytypism.

In particular defect situations irregularly condensed five-membered clusters were found. They are characterized by a fifth Mo octahedron which is *cis*-edge condensed to the second and third octahedron of a common tetrameric cluster.

ACKNOWLEDGMENTS

The authors are greatly indebted to Dr. George L. Schimek and Dr. Dick E. Nagaki for preparing the investigated crystals and to Miss Viola Duppel for her assistance with the microscopy work and the design of figures.

REFERENCES

1. J. G. Allpress, J. V. Sanders, and A. D. Wadsley, *Phys. Status Solidi* **25,** 541 (1968).
2. R. Gruehn and W. Mertin, *Angew. Chem. Int. Ed. Engl.* **19,** 505 (1980).
3. G. L. Schimek, D. E. Nagaki, and R. E. McCarley, *Inorg. Chem.* **33,** 1259 (1994).
4. A. Simon, *Angew. Chem. Int. Ed. Engl.* **27,** 159 (1988).
5. K.H. Lii, C. C. Wang, and S. L. Wang, *J. Solid State Chem.* **77,** 407 (1988).
6. G. L. Schimek and R. E. McCarley, *J. Solid State Chem.* **113,** 345 (1994).
7. C. C. Torardy and R. E. McCarley, *J. Solid State Chem.* **37,** 393 (1981)
8. C. C. Torardy and R. E. McCarley, *J. Less Common Met.* **116,** 169 (1986).
9. R. Ramlau, *J. Solid State Chem.* **130,** 290 (1997).
10. C. C. Torardy and R. E. McCarley, *J. Am. Chem. Soc.* **101,** 3963 (1979).
11. R. Ramlau, E. Fais, Hj. Mattausch, and A. Simon, *Optik* **94**, Suppl. 5, 70 (1993).
12. R. Ramlau, G. Schimek, R. E. McCarley, and A. Simon, *Z. Anorg. Allg. Chem.* **622,** 437 (1996).
13. P. A. Stadelmann, *Ultramicroscopy* **21,** 131 (1987).
14. R. A. Ploc and G.H. Keech, *J. Appl. Crystallogr.* **5,** 244 (1972).
15. A. Guinier *et. al.*, *Acta Crystallogr. A* **40,** 399 (1984).
16. R. Dronskowski, Hj. Mattausch, and A. Simon, *Z. Anorg. Allg. Chem.* **619,** 1397 (1993).
17. E. Fais, H. Borrmann, Hj. Mattausch, and A. Simon, *Z. Anorg. Allg. Chem.* **621,** 1178 (1995).
18. P. Gougeon, M. Potel, and M. Sergent, *Acta Crystallogr. C* **46,** 1188 (1990).
19. R. Dronskowski and A. Simon, *Angew. Chem. Int. Ed. Engl.* **28,** 758 (1989).
20. G. L. Schimek, S. C. Chen, and R. E. McCarley, *Inorg. Chem.* **34,** 6130 (1995).
21. R. Ramlau, A. Simon, and R. E. McCarley, *Microsc. Microanal.* **3,** Suppl. 2, 639 (1997).